Applied Thermal Engineering 244 (2024) 122712

Contents lists available at ScienceDirect

Applied Thermal Engineering

journal homepage: www.elsevier.com/locate/apthermeng

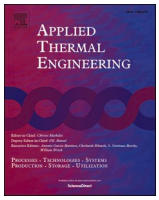

Research Paper

Generation of compressed air by overdriven free-displacer thermocompressors – Experimental investigation of a single stage

Fabian Fischer, Hans-Detlev Kühl *

Technische Universität Dortmund, Lehrstuhl für Thermodynamik (BCI), Emil-Figge-Straße 70, 44227 Dortmund, Germany

ARTICLE INFO

Keywords:
Reciprocating thermocompressor
Thermal compression
Compressed air
Waste heat utilization
Overdriven mode
Stirling cycle

ABSTRACT

A thermocompressor cascade of identical stages has been identified as a promising approach to utilize waste heat for the direct generation of compressed air. This contribution presents the first design, realization and experimental investigation of a single-stage prototype featuring a free displacer oscillating in overdriven mode, which has so far only been devised and analyzed theoretically and by simulations. It is self-excited by the p,V-work generated by its rod, which periodically plunges into the cold cylinder volume. In general, the experimental performance confirms the expectations, as a stable, self-controlled operation is possible within a wide range of pressure ratios and inlet pressure levels. However, the theoretical maximum pressure ratio, at which the machine would inevitably stop, is not reached experimentally. Instead, operation continues at a lower pressure ratio, where the net mass flow drops to zero due to leakage effects. This behavior could be confirmed by an enhanced numerical model. In addition, an automatic, self-excited start by decreasing the pressure ratio could be experimentally confirmed. This is a typical industrial operating scenario, when compressed air is fed to a reservoir and consumption increases. These promising findings strongly suggest the realization and testing of a multi-stage cascade as the next step.

1. Introduction

Compressed air is used in a wide range of industrial applications, but since its generation and utilization are often rather inefficient, it is energy-intensive and therefore expensive and environmentally unfriendly [1]. At the same time, several studies have shown that huge amounts of industrial waste heat are not utilized at all up to now [2–5]. Fischer and Kühl [6] propose to exploit this waste heat potential by direct generation of compressed air using so-called reciprocating thermocompressors, which are closely related to Stirling engines, but until now their concept was only investigated analytically and numerically.

The general idea of compressing gases by thermal effects dates back to a patent granted to Vannevar Bush in 1935 [7]. This is why such machines are sometimes referred to as "Bush Compressors". In the past, most research has focused on the analytical and numerical modeling of thermocompressors. Detailed literature overviews can be found in [6,8], and [9]. However, some constructive approaches to the realization of thermocompressors have also been published. In general, these machines may be divided into two categories, as some realize an open cycle, while the rest constitute closed systems and therefore do not comply with the original concept by Bush. The second group is often intended to be used as compressors for pulse-tube coolers [10], heat pumps [11], and refrigerators [12], or the working gas is sealed off from the conveyed fluid, as in the concepts by Eder [10,13] and Riofrio [14,15] or the experiments related to the actuation of artificial hearts during the 1960s and 1970s [16,17].

Detailed experimental results obtained from the operation of generally similar, but externally driven thermocompressors are presented by several authors [11,18–23]. However, even though some of the machines are basically equipped with valves to realize an open cycle, these have generally been blocked, so that all experiments were carried out with a closed system. Furthermore, these studies have in common that helium or nitrogen is used as working gas. In summary, these were far from being able to replicate the operation of a typical industrial compressed air system.

Only few contributions follow Bush's original idea of directly compressing and conveying gas by a thermocompressor. Above all, Glassford [24] should be mentioned here. He experimentally investigated a very simple, externally driven thermocompressor with the intent to generate oil-free compressed air. The experiments prove the feasibility of the concept, but due to the simple and rather inaccurate manufacturing

* Corresponding author.
E-mail address: hans-detlev.kuehl@tu-dortmund.de (H.-D. Kühl).

https://doi.org/10.1016/j.applthermaleng.2024.122712
Received 23 October 2023; Received in revised form 16 January 2024; Accepted 12 February 2024
Available online 13 February 2024

Nomenclature

A	Cross-sectional area, m^2
B	Sum of the temperature-related mean volumes, m^3/K
C	Spring stiffness
c_p	Isobaric heat capacity, J kg^{-1} K^{-1}
d	Diameter, m
D	Sum of the temperature-related volume amplitudes, m^3/K
E	Exergy, J
F	Constant factor, kg s^{-1} Pa^{-2}
g	Relative change of the exergy flow, –
h	Specific Enthalpy, J kg^{-1}
j	Viscous friction coefficient, N s/m
l	Length, m
m	Mass, kg
n	Number
N	Operating frequency, Hz
p	Pressure, Pa
Q	Heat, J
R	Specific gas constant, J kg^{-1} K^{-1}
T	Temperature, K
t	Time, s
V	Volume, m^3
v	Velocity, m/s
W	Work, J
x	Position, m

Greek letters

δ	Damping constant, –
Δ	Difference
η	Regenerator effectiveness
θ	Temperature ratio, –
λ	Thermal conductivity
Π	Pressure ratio, –
ρ	Ratio of cross-sectional areas of displacer and rod, –
σ	Dimensionless temperature-related dead volume, –

Dimensionless numbers

NTU	Number of Transfer Units
Re	Reynolds number

Superscripts

$\dot{x}$	Time derivative
$\overline{x}$	Mean
$\widehat{x}$	Amplitude

Subscripts

add	Additional
amb	Ambience
C	Cylinder
c	Cold
cyc	Cycle
D	Displacer
d	Value in a dead Volume component
h	Hot
i	Component number
id	ideal
in	Inlet
k	Stage number
leak	Leakage
lim	Limit (practical)
max	Maximum (theoretical)
opt	Optimum operating point
out	Outlet
P	Power
R	Rod
r	Regenerator
sh	Shuttle

techniques that had been applied to realize his prototype, the performance of the machine was poorer than expected. Thomas and Barth [9,25] reused the machine described in [22], but connected it to two pressure reservoirs, which were equipped with two check valves. Starting at a common initial pressure, helium was conveyed from one reservoir to the other. The authors compared the power output obtained by sinusoidal and square wave motion profiles at different frequencies of 1–2 Hz.

The maximum pressure ratio of a thermocompressor is limited by the temperature ratio and further reduced by unavoidable dead volumes. Moreover, the actual operating pressure ratio must be even lower to convey air. So, multiple stages are required to achieve industrially relevant pressure levels of 6–10 bar. Due to the relatively low power density, such a machine has to be as constructively simple and cost-effective as possible to be competitive in the market. Thomas and Barth [26] therefore suggested connecting multiple identical stages via a common crankshaft and thus operating them at a common frequency. In this case, the challenge is the constraint of a constant mass flow along the cascade, even though the gas mass conveyed per cycle increases linearly with the inlet pressure of each stage, but decreases with the pressure ratio. Therefore, the first stage will operate at a low pressure ratio, and the last stage will operate close to the maximum, so that only a few stages will operate at their optimum operating point regarding the exergy gain of the compressed air flow. To overcome this challenge, Fischer and Kühl [6] suggested using overdriven free displacers instead.

In this case, the frequency of each stage depends on the operating point, i.e. on the pressure ratio, since the p,V-work generated by the change in total volume due to the immersion of a displacer rod in the cold cylinder volume of the machine is used for actuation. At a stable operating point, this p,V-work must compensate all losses, especially those due to flow friction. This arrangement allows the operating frequencies to vary inversely to the stage pressure and thus to run all the stages close to their optimum operating point. It turns out that such a variation results in a far-reaching similarity in terms of heat transfer, as relevant dimensionless numbers such as Reynolds, Valensi, and Nusselt numbers remain constant. Until now, this concept has been studied by an isothermal analysis of a single stage, with a particular focus on the displacer motion. Furthermore, the existence of stable operating points for a multi-stage cascade has been proven analytically and numerically [27].

This contribution presents the first experimental realization of a single-stage thermocompressor with an overdriven free displacer, of which only a general design concept was presented in [28]. This machine has been experimentally tested in various operating states, including those of the higher stages of a cascade, i.e. at elevated inlet pressures above the ambient pressure p_0. For this purpose, a test stand has been developed, which is connected to the compressed air network of the laboratory so that in contrast to the latest works in the field a realistic open system is set up and air is used as the working gas. Furthermore, the test stand allows the simulation of typical industrial compressed air use cases, such as operation at a constant pressure ratio due to a constant demand or a sudden demand after reaching a maximum pressure level before. This demonstrated the feasibility of the concept, which had only been modeled analytically and numerically before. Therefore, such a system is expected to be capable of replacing or at least supplementing conventional compressors and thus reducing the

primary energy demand for compressed air generation. In addition, the analytical single-stage model presented in [6] is extended to include several loss mechanisms such as heat transfer, conduction, regeneration and flow pressure losses, and it is successfully validated by the experimental results to provide a tool for the future development of a cascade.

2. The thermocompressor cycle

Fig. 1 shows the basic layout of a single-stage thermocompressor, as investigated experimentally in this contribution. Since a displacer piston divides a cylinder into a cold and a hot volume, it shows structural similarities to a β- or γ-type Stirling engine, but the working piston known from Stirling engines is replaced by a pair of check valves, which connect the cold cylinder volume to an inlet and an outlet buffer. Therefore, the cycle is open, and air acts as both the working fluid and the product stream. Inside the machine, it is displaced between these two cylinder volumes via a cooler, a regenerator and a heater. The displacer rod is located in the cold cylinder volume. The stepped rod plunges into both buffer volumes with equal shares of its cross-section, so that it is equally exposed to the inlet and outlet pressure. Therefore, in total the mean pressure acts on the rod. Via the nozzles, the stage can be connected to larger additional buffers or adjacent stages. A mechanical spring of customized stiffness compensates for the weight of the displacer and equalizes the overall forces during the cycle advantageously. Due to its design as an overdriven free displacer, elastic limit stops are required at the ends of stroke to reverse its direction as lossless as possible.

Fig. 2 shows an exemplary p,V-diagram of the ideal thermocompressor cycle, which can be characterized by a sequence of four processes described in detail by Glassford [29], Karabulut [30] or Fischer and Kühl [6], among others. Since the total volume is not changed except by the piston rod plunging into the cold cylinder volume, the p,V loops for the hot and the cold cylinder volume are almost mirror images of each other, and the loop area for the total volume is very small. During processes 1–2 and 3–4, all valves are closed, so that the system gas mass is constant and undergoes a thermal compression or decompression, respectively. Unlike a Stirling cycle, the thermocompressor cycle is open, so that gas is isobarically conveyed out of or into the system during process 2–3 and process 4–1, respectively.p_{k-1} and p_k

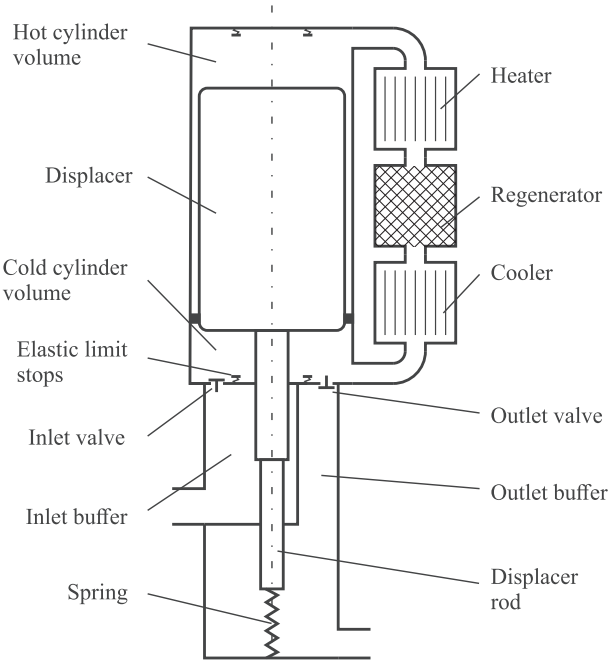

Fig. 1. Schematic drawing of an overdriven free-displacer thermocompressor.

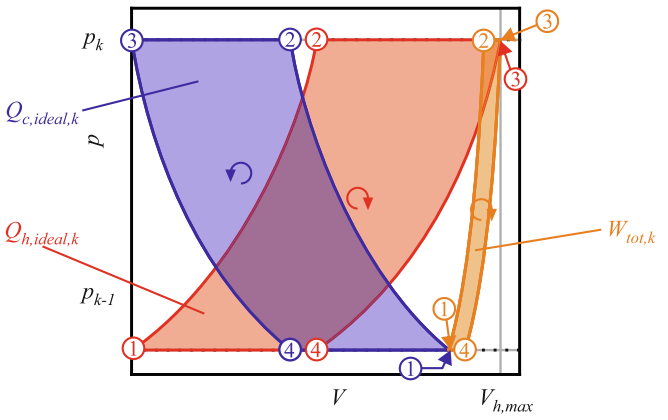

Fig. 2. Ideal p,V-loops for the cold cylinder volume (blue), the hot cylinder volume (red) and the total volume (orange).

denote the inlet and outlet pressure of a stage k. The enclosed areas correspond to the amounts of heat ideally transferred via the cylinder volumes, $Q_{h,ideal}$ and $Q_{c,ideal}$, and to the ideal work W_{tot}, respectively.

Adapting the well-known Schmidt theory of the Stirling cycle, Fischer and Kühl [6] derived an analytical model accounting for an arbitrary number of dead volumes, different temperature levels, and the effect of the displacer rod. This model can be used to calculate the absorbed heat of the ideal isothermal cycle [29]:

$$Q_{h,ideal,k} = p_{k-1}\ 2\ \widehat{V}\ \frac{\Pi_{max} - \Pi_k}{\Pi_{max} - 1}\ \ln\Pi_k \tag{1}$$

Here, $\widehat{V}$ the volume amplitude of the hot cylinder volume, $\Pi_k = p_k/p_{k-1}$ the pressure ratio and Π_{max} the maximum possible pressure ratio, when the inlet and outlet valves do not open anymore and no gas mass is conveyed. This maximum pressure ratio

$$\Pi_{max} = \frac{B + D}{B - D} \tag{2}$$

is theoretically limited by the temperature levels and the geometry of the machine, since it only depends on the mean sum of the temperature-related volumes

$$B = \frac{\widehat{V}}{T_c}(1 - \rho + \theta + \sigma) \tag{3}$$

and its amplitude

$$D = \frac{\widehat{V}}{T_c}(1 - \rho - \theta) \tag{4}$$

Both are functions of the cold temperature T_c, the ratio of the cross-sectional area of the displacer rod A_R and the displacer A_D

$$\rho = \frac{A_R}{A_D}, \tag{5}$$

the ratio of the cold and the hot temperature

$$\theta = \frac{T_c}{T_h} \tag{6}$$

and the sum of the temperature-related dead volumes $V_{d,i}$ of each component i

$$\sigma = \frac{T_c}{\widehat{V}} \sum \frac{V_{d,i}}{T_{d,i}} \tag{7}$$

The shape of the course of Eq. (1) for the full operating range $1 < \Pi < \Pi_{max}$ is similar to an inverted parabola with zeros at $\Pi = 1$ and $\Pi = \Pi_{max}$

and a maximum occurring approximately at the geometrical mean of these zeros, i.e. $\Pi_{opt} \approx \sqrt{\Pi_{max}}$. Since the work generated per cycle,

$$W_{R,k} = \rho \; Q_{h,ideal,k} \tag{8}$$

as well as the exergy transferred to the conveyed air flow are proportional to the heat $Q_{h,ideal,k}$ absorbed by the ideal cycle according to Eq. (1), this maximum is the optimum operating point. The work generated per cycle must compensate the dissipation by viscous fluid friction, which is linearly speed-dependent. So, the frequency at a stable operating point features the same dependencies as $Q_{h,ideal}$:

$$N_k \; p_{k-1}(\Pi_{max} - \Pi_k)\ln\Pi_k \tag{9}$$

The aforementioned quantities furthermore allow the calculation of the mass of air conveyed per cycle:

$$\Delta m_k = p_{k-1}(\Pi_{max} - \Pi_k)\frac{B - D}{R} \tag{10}$$

In a cascade, the mass flow $\dot{m}$ in two consecutive stages k and $k+1$ must be the same:

$$\dot{m} = N_k \Delta m_k = N_{k+1} \Delta m_{k+1} = const. \tag{11}$$

Assuming that both stages initially operate at the optimum pressure ratio Π_{opt}, stage $k+1$ will convey a larger mass flow than stage k, since we have both $N_{k+1} > N_k$ and $\Delta m_{k+1} > \Delta m_k$ due to the higher inlet pressure. Consequently, the pressure ratio Π_{k+1} will increase beyond $\Pi_k = \Pi_{opt}$. In this case, both N_{k+1} and Δm_{k+1} decrease, but whereas the decrease of Δm_{k+1} is linear according to Eq. (10), that of N_{k+1} is less due to the additional effect of the logarithm in Eq. (9). So, Eq. (11) can only be fulfilled by a combination of $\Delta m_{k+1} < \Delta m_k$ and $N_{k+1} > N_k$. Therefore, the operating frequency of a subsequent stage will always be somewhat higher than that of the preceding stage in steady-state operation.

The similarity with respect to the heat transfer conditions mentioned in the introduction, which requires the frequency to vary inversely with the stage pressure and which was initially anticipated because of the decreasing generation of p,V work at pressure ratios above Π_{opt} [6], is evidently not fulfilled according to this result. The Reynolds number will gradually rise from stage to stage due to increasing pressure and frequency values, but the Nusselt number will be hardly affected in case of laminar flow, and thus, the heat transfer coefficients will essentially remain constant or may eventually even rise slightly, too. On the other hand, any stage k delivers an exergy flow

$$\Delta \dot{E}_k = \dot{m} \; R \; T_{amb} \; \ln\Pi_k \tag{12}$$

to the compressed air flow, which is presumably the most appropriate criterion for its performance. If a constant ambient temperature T_{amb} and a constant mass flow $\dot{m}_{air}$ is assumed, it is exclusively dependent on Π_k. Therefore, any subsequent stage $k+1$ will perform better that the preceding stage k, since we always have $\Pi_{k+1} > \Pi_k$ according to the above considerations, even though the increased load on the heat transfer surfaces may result in additional losses and thus a marginally decreased real performance of stage $k+1$.

This finally confirms the previous finding that the first stage of a cascade is most critical for the overall performance [6]. Therefore, any design optimization must be done for the minimum inlet pressure p_0, and the overall number of stages must be chosen so that the first stage operates at a pressure ratio $\Pi_1 \approx \Pi_{opt}$.

3. Experimental machine and test stand

As a first step to experimentally demonstrate the feasibility of a thermocompressor cascade with overdriven free-displacers as suggested by Fischer and Kühl [6] and summarized in section 2, a single stage was designed and constructed. In contrast to the more complex design shown in Fig. 1, which connotes a radially shifted arrangement of heat exchangers and a regenerator as separate components, a concentric design was realized in the experimental machine, thus avoiding additional connecting ducts. This was mainly motivated by the reduction of dead volume and flow pressure losses, which both have an extremely negative impact on the machine performance and should be minimized by all means [6]. Furthermore, this concept favors the demand for a constructionally simple, low-cost machine design [28] and complies with Walker's recommendation to replace complex heat exchangers and regenerators by an annular gap in small-scale machines operating below 500 rpm and at low pressures [31]. Lin et al. [19,20], Winkelmann and Barth [22] as well as Thomas and Barth [9,25] also chose this approach and generally obtained good results.

The cylinder comprises three segments representing the cooler, the regenerator, and the heater as illustrated in Fig. 3. The cooled segment consists of an inner aluminum cylinder with radial fins and an outer sleeve forming a water jacket, which is connected to a circulatory. In Fig. 4 a photo of the experimental machine and the test stand is provided.

In the regenerator segment, the cylinder wall is made from stainless steel because of its relatively low thermal conductivity. In between the two connecting flanges, its wall thickness was reduced to 1.15 mm, which is the lower limit imposed by the prototype machining process, not by stability. In series production, the wall thickness – and thus the thermal conduction losses – may be further reduced by applying more efficient and advantageous manufacturing methods such as deep drawing.

To ensure a homogeneous temperature distribution, the heater segment consists of a solid cylindrical block made from aluminum once again. An electric heating wire with 400 W maximum power is inserted in a spiral groove around its outer circumference and kept in place by a surrounding sleeve.

These three segments are mounted on a cylinder base plate, which separates the active cycle volume from the inlet and outlet buffers. The displacer rod is guided by two bushings made from low-friction plastic IGUS iglidur H370, which are inserted in the cylinder base plate and the wall between the buffers. For reasons of commercial availability, their diameters were chosen as $d_{r,1} = 20$ mm and $d_{r,2} = 14$ mm, respectively.

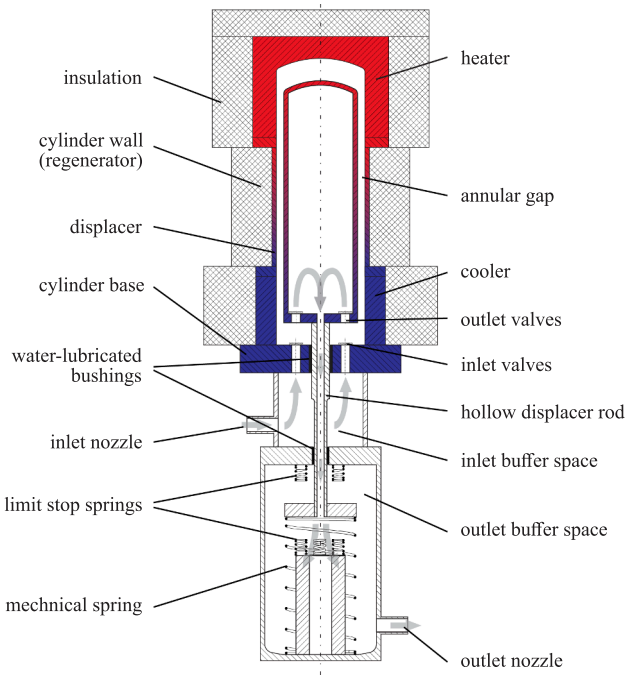

Fig. 3. Schematic sketch of the experimental machine (based on [28]).

Fig. 4. Photo of the experimental machine and the test stand.

Thus, the cross section ratio of 2:1 suggested for an optimum force balancing [6] is approximated fairly well. Due to the different thermal expansion of the bushings and the displacer rod, the close-tolerance fits had to be adjusted manually to minimize leakage losses.

During steady-state operation of a multi-stage cascade, water will inevitably condense in the higher stages, since its partial pressure will exceed the saturation pressure due to the quasi-isothermal compression of the humid intake air. This condensation is expected to primarily occur in the outlet buffers, since the gas temperature in these will be below the exit temperature of the cycle due to the additional heat rejection via their large surface. This water, which will accumulate in their sump, may be profitably used for lubrication and sealing purposes in the bushings. It can easily be transferred to the center of their gaps via filters, capillaries, and radial bores in each bushing due to the existing pressure difference. Finally, it will accumulate in the sump of the inlet buffer and exit the stage via the inlet nozzle in counterflow to the intake air. In a multi-stage cascade, the water will thus be consecutively transferred from the higher to the lower stages, so that a sufficient water supply is also ensured in the latter even if no water is condensing in these. To simulate this effect during the operation of a single-stage prototype, a small stream of water is externally supplied to its outlet buffer.

The gap width around the displacer is $s_{gap} = 1.2$ mm, and its diameter is $d_D = 82.5$ mm, resulting in a displacer-rod-ratio of $\rho = 0.0588$. The displacer dome is made of stainless steel for the same reason as the cylinder wall and consists of a cap, a seamless tube, and a flange to mount it on the displacer base. The final diameter of the displacer is achieved by lathing after soldering the three components to ensure accuracy. The resulting displacer wall thickness is $s_D = 1.15$ mm and is once again limited by the manufacturing process rather than by the small pressure difference. The cooled cylinder length amounts to $l_c = 88$ mm, the heated length is $l_h = 85$ mm. All geometrical parameters are summarized in Table 1.

It is well known from the field of conventional piston compressors that valve design has a huge impact on the performance of the machine [32,33]. To minimize flow pressure losses, the cylinder base therefore exclusively accommodates the inlet valves to maximize their number (4) and thus their total cross-sectional area. The four outlet valves are instead accommodated in the displacer base. Thus, the air can flow into the outlet buffer via the interior of the displacer and the hollow rod, as indicated in Fig. 3. All valves are designed as self-acting reed valves. Preliminary tests yielded best results for silicone reeds in combination with retainers to optimize opening behavior and dynamics.

Table 1
Summary of the geometrical dimensions of the experimental machine.

Quantity	Symbol	Value
Max. stroke amplitude	$\hat{x}$	25 mm
Displacer diameter	d_D	82.5 mm
Displacer wall thickness	s_D	1.25 mm
Displacer length	l_D	256 mm
Annular gap width	s_{gap}	1.2 mm
Cylinder wall thickness	s_C	1.15 mm
Cooler length	l_c	88 mm
Heater length	l_h	85 mm
Displacer rod diameter 1	$d_{r,1}$	20 mm
Displacer rod diameter 2	$d_{r,2}$	14 mm
Inlet valve hole diameter	$d_{v,in}$	8.5 mm
Outlet valve hole diameter	$d_{v,out}$	5.5 mm
Number of inlet valves	$n_{v,in}$	4
Number of outlet valves	$n_{v,out}$	4
Length bushing 1	l_{b1}	35 mm
Length bushing 2	l_{b2}	25 mm
Displacer mass	m_D	2.1 kg
Spring constant	C_S	0.1 N/mm

The upper and lower elastic limit stops are realized by four sufficiently stiff spiral springs each, which are located in the outlet buffer and hit by a steel disk mounted at the end of the displacer rod. This disk is also used to mount a mechanical spring of stiffness 0.1 N/mm, corresponding to half the absolute value of the estimated (negative) cycle gas spring constant at an inlet pressure $p_0 = 1.01$ bar. Instead, the additional gas spring suggested in [6] was omitted. This deviation from the original design constitutes a further constructional simplification, as the additional effort for sealing and control of the mean pressure is avoided. The entailed violation of the general similarity concept is marginal, since the effect of the gas spring stiffness on the displacer motion is comparatively small [27]. In addition, a preloaded mechanical spring is anyway required to compensate the weight of the displacer. Due to the low cycle spring constant, this mechanical spring will significantly add to the total spring constant and thus disturb the similarity in any case.

Fig. 5 shows a schematic flow chart of the test stand with the thermocompressor as its central element. The heater and cooler temperatures are monitored and controlled. The heater and the cooling water temperatures are measured by axially distributed thermocouples and by a resistance thermometer, respectively. Additionally, the cycle pressure is measured by a piezoresistive absolute pressure sensor mounted in the cold cylinder volume. The displacer position is monitored via a linear variable differential transformer (LVDT), the plunger of which is attached to the lower end of the displacer rod. This measurement equipment is not included in Fig. 3. The types and accuracies of all installed sensors and the data acquisition modules used are listed in Table A-1 and Table A-2. Before taking a measurement series, the pressure signals were calibrated by comparison to a high-precision reference at ambient pressure. Therefore, the error in pressure measurements could be reduced to a minimum well below the specified sensor accuracy [34], especially since the measured pressures were close to the calibration pressure. The error in the gas flow measurements was reduced by switching between two sensor operating modes with different calibrated ranges, each of which features the same relative error according to the vendor's datasheet. The first one ranges from 0 to 4 l_n/min and the second from 0 to 20 l_n/min, so the latter was only used for gas flows above 4 l_n/min. To further reduce errors due to the non-repeatability of the sensors and of course, the cycle itself, all measured variables were averaged over 5 full cycles.

Additional buffers are installed upstream and downstream of the machine to reduce pressure fluctuations due to the cyclic air inlet and outlet. The upstream buffer pressure can be controlled by a pressure

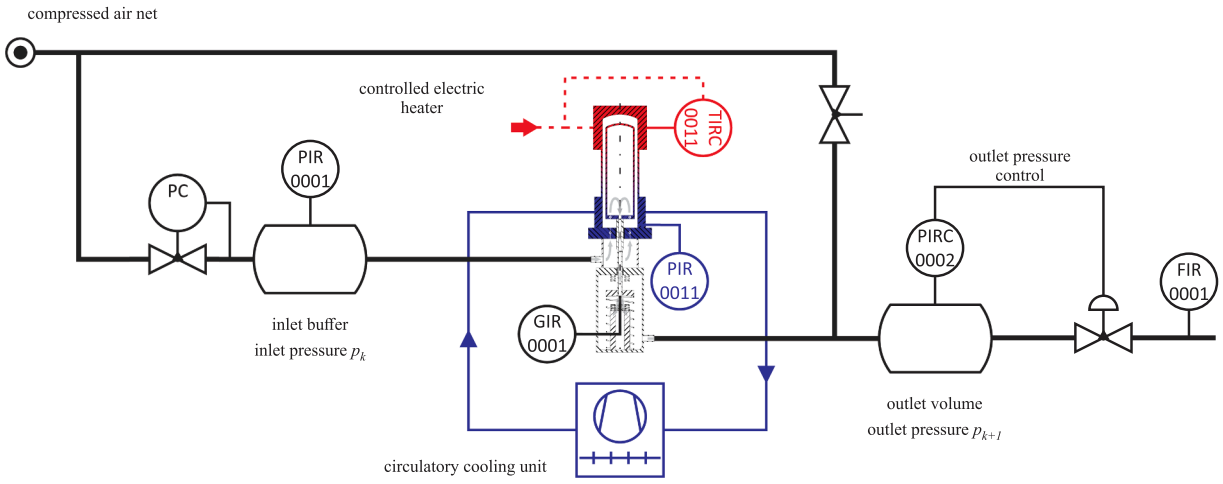

Fig. 5. Schematic flow chart of the test stand.

regulator attached to the compressed air supply of the lab, so that the machine can be operated at higher inlet pressures p_0, similar to a higher stage of a cascade. It is measured by a piezoresistive absolute pressure sensor. The outlet buffer pressure p_1 downstream of the machine is also measured and controlled by a software-controlled solenoid control valve to maintain a preset pressure ratio. In combination with the measurement of the delivered air mass flow by a high-precision thermal mass flow meter, all quantities required to record operating curves are measured. Especially for starting up the machine, a bypass is required to fill the outlet buffer directly and thus apply a preset pressure ratio. The program for data acquisition, logging and control is implemented in NI LabVIEW.

4. Mathematical model

The machine was designed using a time-averaged second-order model, which is visualized in Fig. 6. It is based on the isothermal model presented in [6] and briefly summarized in section 2, but includes convective heat transfer between the walls and the gas and several additional loss mechanisms. Within the model, the machine is subdivided into three sections with a uniform gas temperature each. The gas temperatures in the hot and the cold section are $T_{h,gas}$ and $T_{c,gas}$, respectively. The gas temperature inside the gap in the insulated center section of the cylinder, which is considered to act as a regenerator, is assumed to be the logarithmic mean temperature $T_{r,gas} = (T_{h,gas} - T_{c,gas})/ln(T_{h,gas}/T_{c,gas})$. For the calculation of the convective heat transfer, the hot and the cold section are subdivided into a cylinder volume and the heater or cooler, respectively. For the resulting geometries, in particular the length of each component, the displacer is assumed to be in the center position, as depicted in Fig. 6. This corresponds to the mean position in case of a symmetric displacer motion, which is therefore applicable, considering a triangular function as it is achieved according to [6] for a sufficiently high displacer mass. The resulting geometrical quantities are listed in Table 2.

The heat transfer coefficients α_h, α_c and α_r are calculated separately for the heater, cooler, and regenerator following [35] for concentric annular gaps. The mean gas velocities, which are necessary input parameters for the correlations, are calculated by determining the periodically displaced gas mass across the center of each component. For the heat transfer coefficients $\alpha_{h,C}$ and $\alpha_{c,C}$ in the hot and cold cylinder volumes a simplification of Woschni's correlation [36] is applied.

The model includes the following thermal losses:

- Regenerator loss
- Shuttle loss

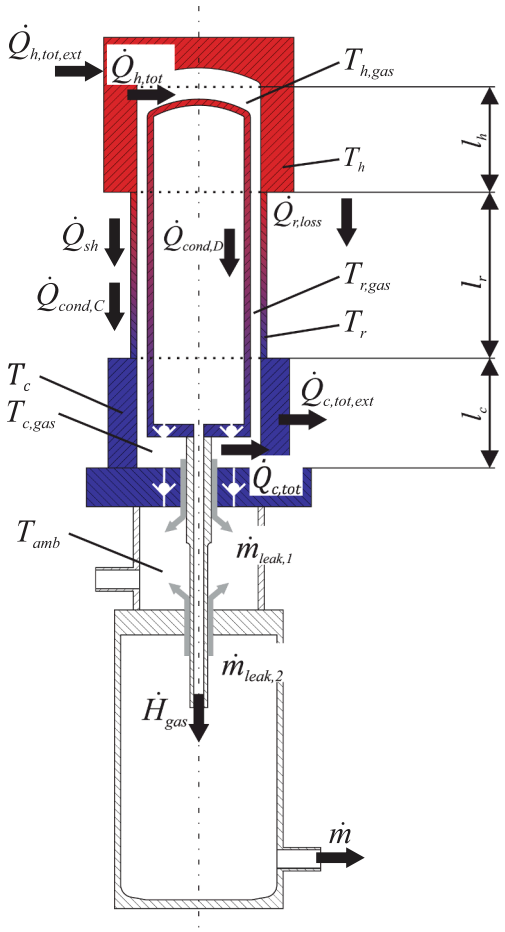

Fig. 6. Visualization of the model including the lengths of the components, heat and enthalpy flows, and temperatures.

- Conduction via the cylinder wall
- Conduction via the displacer wall

The heat flow that has to be additionally supplied due to regenerator losses can be obtained by

$$\dot{Q}_{r,loss} = (1 - \eta_r)\dot{Q}_{r,id} \tag{13}$$

Table 2
Geometrical information about the components included in the model.

Component	Mean surface area	Dead volume
Hot cylinder volume	$\overline{A}_{h,C} = f_{h,C}\pi/4d_C^2 + \pi d_C\widehat{x}$	$V_{d,h,add}$
Heater	$\overline{A}_h = \pi d_C(l_h - \widehat{x})$	$V_{d,h} = \pi/4\left(d_C^2 - d_D^2\right)(l_h - \widehat{x})$
Regenerator	$\overline{A}_r = \pi d_D l_r + \pi d_C l_r$	$V_{d,r} = \pi/4\left(d_C^2 - d_D^2\right)l_r$
Cooler	$\overline{A}_c = \pi d_C(l_c - \widehat{x})$	$V_{d,c} = \pi/4\left(d_C^2 - d_D^2\right)(l_c - \widehat{x})$
Cold cylinder volume	$\overline{A}_{c,C} = f_{c,C}\pi/4d_C^2 + \pi d_C\widehat{x}$	$V_{d,c,add}$

η_r is the regenerator efficiency and $\dot{Q}_{r,id}$ the heat flow in case of ideal regeneration [37]. The regenerator efficiency is calculated as

$$\eta_R = 1/(1 + NTU/2) \tag{14}$$

The number of transfer units,

$$NTU = \frac{\alpha_r\ \overline{A}_r}{2\ N\ \Delta m_r\ c_{p,r}} \tag{15}$$

is a function of the heat transfer coefficient within the regenerator gap α_r, the mean regenerator surface $\overline{A}_r$, the operating frequency N, the isobaric heat capacity $c_{p,r}$ of the air at the gas temperature $T_{gas,r}$, and the periodically displaced mass Δm_r.

According to Urieli and Berchowitz [37], the shuttle loss caused by the periodically moving displacer wall can be estimated as

$$\dot{Q}_{sh} = \frac{\pi}{2} d_D\ \widehat{x}^2\ \frac{\lambda_{air,r}}{s_{gap}}\ \frac{T_{h,gas} - T_{c,gas}}{l_D} \tag{16}$$

Here, in addition to the aforementioned quantities, $\lambda_{air,r}$, s_{gap} and l_D denote the thermal conductivity of air at $T_{gas,r}$, the width of the annual gap and its length, which is equal to that of the displacer.

The total heat flow $\dot{Q}_{h,tot}$ to be transferred to the gas is the sum of the heat flow $\dot{Q}_h = NQ_h$ absorbed by the cycle according to Eq. (1) and the aforementioned regenerator, shuttle, and displacer conduction losses:

$$\dot{Q}_{h,tot} = \dot{Q}_h + \dot{Q}_{r,loss} + \dot{Q}_{sh} + \dot{Q}_{cond,D} \tag{17}$$

The conduction heat flow via the cylinder wall is not included, as it need not be transferred to the gas. It does, however, add to the total externally supplied heat flow $\dot{Q}_{h,tot,ext}$ according to

$$\dot{Q}_{h,tot,ext} = \dot{Q}_{h,tot} + \dot{Q}_{cond,C} \tag{18}$$

The heat flow $\dot{Q}_{c,tot}$, which is transferred from the gas to the cold section, is evaluated similarly:

$$\dot{Q}_{c,tot} = \dot{Q}_h(1 - \rho) + \dot{Q}_{r,loss} + \dot{Q}_{cond,D} + \dot{Q}_{sh} - N\ \Delta\mathrm{m}\ c_{p,c}\left(T_{c,gas} - T_{amb}\right) \tag{19}$$

However, the effect of the displacer rod and the enthalpy flow due to a temperature difference between the ambient and cold cycle temperatures are taken into account. Here, the conveyed mass per cycle Δm_{air} is calculated according to Eq. (10).

$$\dot{Q}_{c,tot,ext} = \dot{Q}_{c,tot} + \dot{Q}_{cond,C} \tag{20}$$

In steady-state operation, the heat flow that is discharged or supplied via the heat exchangers equals the convective heat flow within the cylinder volumes and the gap.

One of the crucial design aspects of the overdriven free-displacer thermocompressor, which is investigated within this contribution, is its self-sustaining operation. This means that the power generated by the piston rod

$$P_R = N\ \rho\ Q_h \tag{21}$$

in steady-state operation must compensate all frictional losses, which are mainly flow pressure losses $P_{\Delta p}$ within the machine including various loss mechanisms:

- laminar flow pressure losses in the annular gap
- inflow into the annular gap from the cylinder volume
- outflow from the annular gap into the cylinder volume
- valve pressure losses (Carnot's shock loss and deflection)

To additionally calculate the power loss P_b due to sliding friction in the bushings, it is assumed that the annular gaps between the displacer rod and the bushings are entirely filled with water, so that viscous fluid friction prevails. To account for further increases of this loss, which may e.g. be caused by an unknown eccentricity of the gap or other alignment inaccuracies, $f_P \approx 1.5$ is introduced as an empirical factor.

Thus, this approach results in a nonlinear system of equations for the gas temperatures $T_{c,gas}$ and $T_{h,gas}$ and the operating frequency N, which has to be solved numerically:

$$\dot{Q}_{c,tot} - \left(\alpha_{c,C}\ \overline{A}_{c,C} + \alpha_c\ \overline{A}_c\right)\left(T_{c,gas} - T_{c,w}\right) =^{!}\ 0 \tag{22}$$

$$\dot{Q}_{h,tot} - \left(\alpha_{h,C}\ \overline{A}_{c,C} + \alpha_h\ \overline{A}_h\right)\left(T_{h,gas} - T_{h,w}\right) =^{!}\ 0 \tag{23}$$

$$P_R - f_P\left(P_{\Delta p} + P_b\right) =^{!}\ 0 \tag{24}$$

An additional visualization of the solving method is provided in the flowchart in Fig A-1.

Fig. 7 exemplary shows the modeling results for a variation of the annular gap width s_{gap} applying the geometrical data listed in Table A-3. To evaluate its effect, the exergy gain of the compressed air flow $\Delta\dot{E}_{opt}$, the operating frequency N_{opt} and the pressure ratio Π_{opt}, each at the optimum operating point, are plotted vs. s_{gap}. The chosen gap width of $s_{gap} = 1.2$ mm does correspond to the maximum of $\Delta\dot{E}_{opt}$, which is found for $s_{gap} = 1.29$ mm. However, the difference is only about one percent, but the pressure ratio at the optimum operating point and the corresponding maximum pressure ratio are improved, which is important for realizing a significant pressure increase and a wider operating range.

Since the first experiments indicated a significant influence of the leakage flows $\dot{m}_{leak,1}$ and $\dot{m}_{leak,2}$ through the gaps between the displacer rod and the bushings, the model was extended by subtracting these from the conveyed mass flow according to Eq. (10), so that the effective conveyed mass flow results in

$$\dot{m} = N\Delta\mathrm{m} - f_{leak,1}\dot{m}_{leak,1} - f_{leak,2}\dot{m}_{leak,2} \tag{25}$$

The leakage flows $\dot{m}_{leak,1}$ and $\dot{m}_{leak,2}$ are calculated assuming laminar flow through the bushing gaps from the cycle volume and the outlet buffer into the inlet buffer, based on the corresponding pressure differences. In the latter case, this is the full pressure difference of the stage, and in the former case, the difference between the mean cycle pressure and the inlet pressure is applied, although this difference is actually fluctuating throughout the cycle. The challenge here is to precisely quantify the flow regime, since it will be severely affected by eccentricities, alignment errors or surface inaccuracies, which will presumably result in significantly higher leakage flows. To account for these unknown effects, the leakage flows may be adjusted by the empirical correction factors $f_{leak,1}$ and $f_{leak,2}$.

5. Experimental results

5.1. Steady-State operation

5.1.1. Analysis of cyclic measurements results

Fig. 8(a) shows an exemplary p,V-diagram of the hot and the cold cylinder volume for an ambient inlet pressure of 0.98 bar, so that the thermocompressor is operated corresponding to a first stage $k = 1$. The heater and cooler temperatures are $T_h = 295$ °C and $T_c = 8$ °C for all

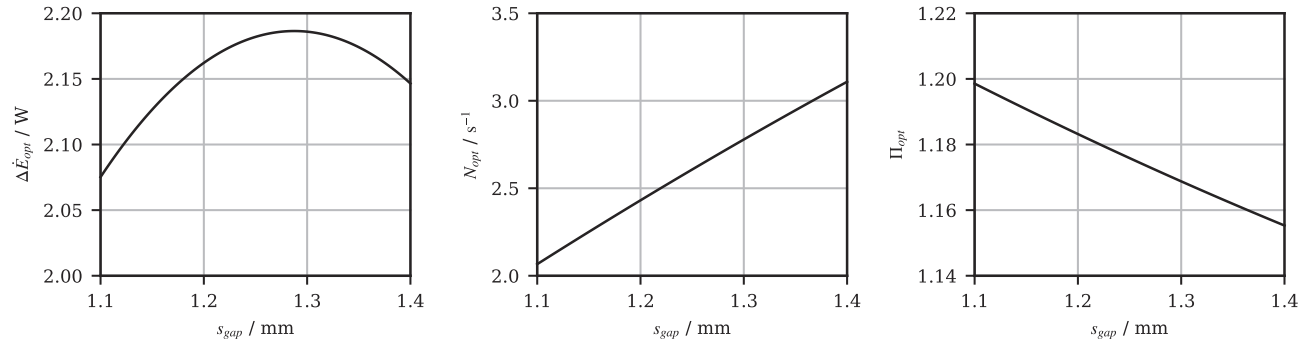

(a) Exergy gain of the compressed air flow (b) Operating frequency (c) Pressure ratio

Fig. 7. Modeling results for the optimum operating point due to a variation of the annular gap width s_{gap} for ambient inlet pressure, a heater temperature $T_h = 295\,^{\circ}\mathrm{C}$ and a cooler temperature $T_c = 8\,^{\circ}\mathrm{C}$.

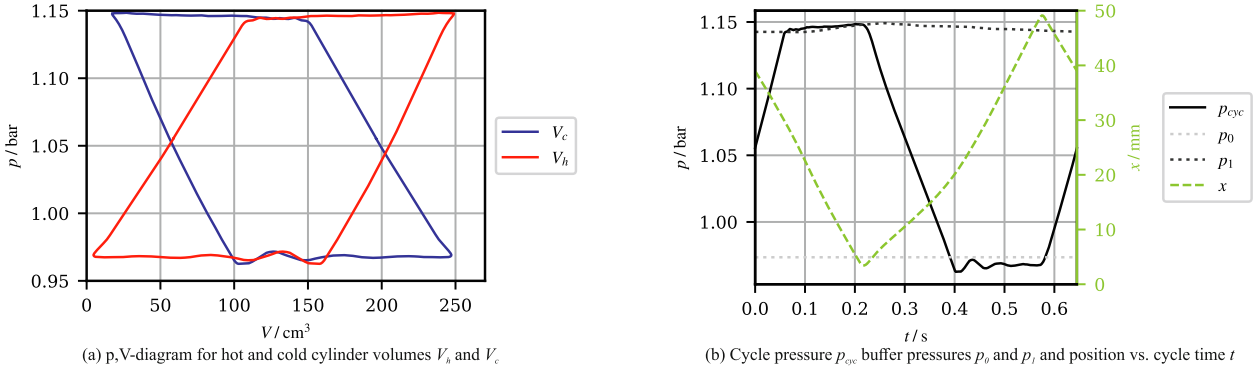

(a) p,V-diagram for hot and cold cylinder volumes V_h and V_c (b) Cycle pressure p_{cyc} buffer pressures p_0 and p_1 and position vs. cycle time t

Fig. 8. Cyclic measurement results for pressure ratio $\Pi = 1.18$ and inlet pressure $p_0 = 0.974$ bar at cooler temperature $T_c = 8\,^{\circ}\mathrm{C}$ and heater temperature $T_h = 295\,^{\circ}\mathrm{C}$ [38].

operating points shown in this contribution. The low cooler temperature was chosen to decrease the temperature ratio without exceeding the maximum heater temperature of 300 °C, which is limited due to a polymer seal in the experimental machine. In an industrial application, both temperatures would presumably be somewhat higher. The pressure ratio Π of an operating point is computed as the ratio of the mean pressures in the outlet and inlet buffer. It is $\Pi = 1.18$ for the displayed operating point, corresponding to Π_{opt} for these conditions.

The general course of the p,V-curves is in good accordance with the schematic course in Fig. 2. All four states and processes are clearly locatable. After the thermal compression, the outlet valves open approximately at the center position of the displacer, which confirms the analytical results in [6]. Please note that the cycle pressure p_{cyc} is only measured in the cold cylinder volume as outlined in section 3. Therefore, the pressure course for the hot volume does not include any flow pressure losses and is merely shown for better comparability to Fig. 2. The discharge is nearly isobaric. The slight increase of the outlet pressure can be explained by minor fluctuations of the outlet buffer pressure p_1, which is plotted vs. the cycle time in addition to the displacer position x, the inlet buffer pressure p_0 and the cycle pressure p_{cyc} in Fig. 8 (b). These fluctuations are caused by the discontinuous inflow of gas via the outlet valves, whereas the outflow via the proportional control valve (Fig. 5) is continuous.

Furthermore, the courses of p_{cyc} and p_1 demonstrate an advantageous characteristic of the outlet valves, as the flow pressure losses are low. The dynamics of the valve is satisfactory as well, as it closes as soon as the displacer hits the lower limit-stop. The general course of the measured displacer motion well matches the analytical predictions [6], especially concerning the progression of the curvature. During the inflow, the cycle pressure shows slight oscillations which are most likely caused by fluttering of the inlet valve reeds, which have an elongated shape to better fit them into the cylinder base, but lack a stopper to avoid additional dead volumes. To reduce the fluttering in future machines, their shape should be adopted to that of the outlet reeds. Nevertheless, the inlet valve characteristics regarding flow pressure losses and dynamics are similar to those of the outlet valves and therefore satisfactory.

5.1.2. *Variation of the pressure ratios at ambient inlet pressure*

Fig. 9 shows the exergy gain of the compressed air per cycle $\Delta E = \Delta\dot{E}/N$, the operating frequency and the gas mass conveyed per cycle Δm for three separate measurement series at ambient inlet pressure. In the following, the results of such measurement series will be referred to as operating curves. By controlling the pressure in the outlet buffer, stable operating states were automatically achieved and the thermocompressor was operated at various preset pressure ratios up to an upper limit of approximately $\Pi_{lim} = 1.3$, where no net mass flow is detected anymore. This value is below the theoretical maximum pressure ratio Π_{max}, which is determined by the geometry of the machine and the temperature ratio and amounts to 1.41 for this machine and the given operating parameters. At this pressure ratio, the valves would not open anymore, so that no p,V-work would be generated and the machine would stop. This pressure ratio cannot be reached experimentally due to the aforementioned leakage flows through the bushing gaps. At the right margin of the operating curve, the mass flow primarily conveyed through the valves is entirely used up by these. Therefore, the net mass flow already drops to zero at a pressure ratio below Π_{max} , where the enclosed area in the p,V-diagram is non zero and the cycle is still generating work.

As a general proof of concept, simulation results for an overdriven single-stage thermocompressor were presented in [27]. These were obtained using a MATLAB®/Simulink® model based on a generally

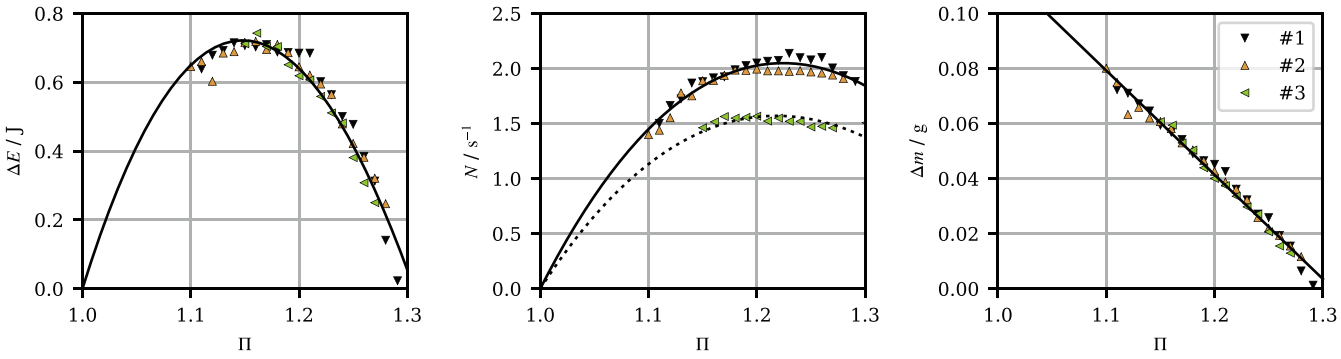

(a) Exergy gain of the compressed air per cycle (b) Operating frequency (c) Mass conveyed per cycle

Fig. 9. Experimental operating curves #1, #2, and #3 according to Table A4 at ambient pressure, a heater temperature of $T_h = 295\,^{\circ}\mathrm{C}$ and a cooler temperature of $T_c = 8\,^{\circ}\mathrm{C}$ and fitted functions [38].

different machine setup with radially shifted heat exchangers and regenerator, but of similar size, i.e. almost the same swept volume. Thus, the performance of the experimental machine is also similar, but reduced by the aforementioned leakages, which were not included in the simulation model. In addition, the simulation results for the frequency were higher because the friction losses were underestimated.

The left margin is caused by stability issues. Since the mass flow drops with decreasing pressure ratio after reaching a maximum at approximately $\Pi = 1.12$, the control of the outlet buffer pressure became unstable below a minimum pressure ratio of $\Pi = 1.1$. This value matches the analytically predicted stability limit Π_{0,K_3}, which is applicable in the case of a single stage with preset inlet pressure according to [27] and yields 1.094 under the given conditions.

In general, the three independently measured operating curves show good reproducibility. Merely the operating frequency N differs for curve #3, because the LVDT sensor was mounted in this case according to Table A-4 and caused additional friction due to a slight misalignment of its plunger. Nevertheless, this solely affects the operating frequency but not the air conveyed per cycle as a function of the pressure ratio.

Functions of the type

$$f(\Pi) = a(b - \Pi)/(b - 1)ln(\Pi) \tag{26}$$

which have the same structure as Eq. (1), have been fitted to the measured data points in Fig. 9(a) and (b) because, according to section 2, both the exergy gain of the compressed air and the p,V-work per cycle, and hence the operating frequency, depend on the absorbed heat Q_h. Evidently, the experimental data can be well reproduced by these functions, which were derived from the isothermal analysis. Similarly, the data for the mass conveyed per cycle confirm the prediction by Eq. (10) and can be well reproduced by

$$f(\Pi) = a(b - \Pi) \tag{27}$$

Considering the exergy transferred to the compressed air flow as the power output of a thermocompressor, the thermal efficiency can be calculated by dividing by the heat supply, which is the electrical power in the case of the prototype. At the optimum operating point $\Pi_{opt} = 1.17$ and ambient inlet pressure, the exergy transferred to the compressed air flow was 1.4 W and the heater power was approximately 185 W, resulting in a thermal efficiency of $\eta_{th} = 0.76\%$, which is relatively poor. However, as mentioned in section 3, the available machining technologies for the prototype were limited, so particularly the wall thickness of the cylinder and the displacer could be reduced to 0.5 mm. This would reduce the conduction losses for operation at the given heater and cooler temperatures by approximately 8.5 W. Additionally, the design of the prototype causes increased thermal losses due to radiation and convection. These losses could be reduced to a minimum, when applying a waste heat enthalpy flow through a well-insulated flow channel along a cascade of thermocompressors. Based on measured surface temperatures of 77 to 92 °C, these losses amount to approximately 120 W, giving the system a corrected efficiency of 2.15 %. Compared to a conventional compressor of similar power available on the market, e.g. Becker DT 4.2 [39], which has an efficiency of up to 33 % and 13 % at $\Pi = 1.17$, the realized efficiency is still low. However, in addition to future improvements in sealing, it is important to note that waste heat is being used instead of electrical energy. As long as fossil energy is at least part of the electricity mix, any reduction in the electricity demand can be interpreted as a reduction of the corresponding fossil fuel demand of a thermal power plant.

The water lubrication of the bushings basically functions in the intended way as described in section 3. However, after around 100 h of operation, the lower bushing showed abrasive wear marks. This is presumably caused by particles arising due to aluminum corrosion. These accumulate in the sump of the inlet buffer, which was originally intended to feed water to the lower bushing. Furthermore, the water flow from the outlet buffer via the bushings to the inlet buffer depends on the absolute pressure difference and was found to rise to more than a liter per hour in case of high inlet pressures. So, the inlet buffer had to be drained regularly, and the water flow that had to be continuously supplied to the machine was far higher than what can be expected to accumulate by condensation of moisture in the highest stage of a cascade.

5.1.3. *Comparison of the experimental data with modeling results*

The comparison of the experimental operating curve #1 with the modeled data shown in Fig. 10 supports the considerations concerning the leakage flows reducing the maximum pressure ratio. By solely adjusting the correction factors $f_{leak,1}$, $f_{leak,2}$, and f_P for leakage and friction losses introduced in section 4, particularly the exergy gain and the mass of the conveyed air per cycle can be well reproduced by the model. For the frequency, the general shape of the curve and the value of the maximum agree with the experiments, but the experimental maximum is shifted to a higher pressure ratio. It is suspected that this discrepancy is caused by the better water transportation from the sump of the outlet buffer to the bushings guiding and sealing the displacer rod, thus improving the lubrication by a reduction of mixed friction effects. In fact, a significantly increased water flow was observed at high pressure differences.

To fit the modeling results to the experimental results as shown in Fig. 10, relatively high values of 14 must be chosen for the correction factors $f_{leak,1}$ and $f_{leak,2}$. However, both a non-uniform gap width and a possible eccentricity of the piston rod have large effects on the mass flow, so these values are plausible. Sufficiently accurate measurements of such deviations from the ideal gap geometry under operating conditions were not possible. The valves have been tested separately for leakage to preclude additional effects. Furthermore, any measured

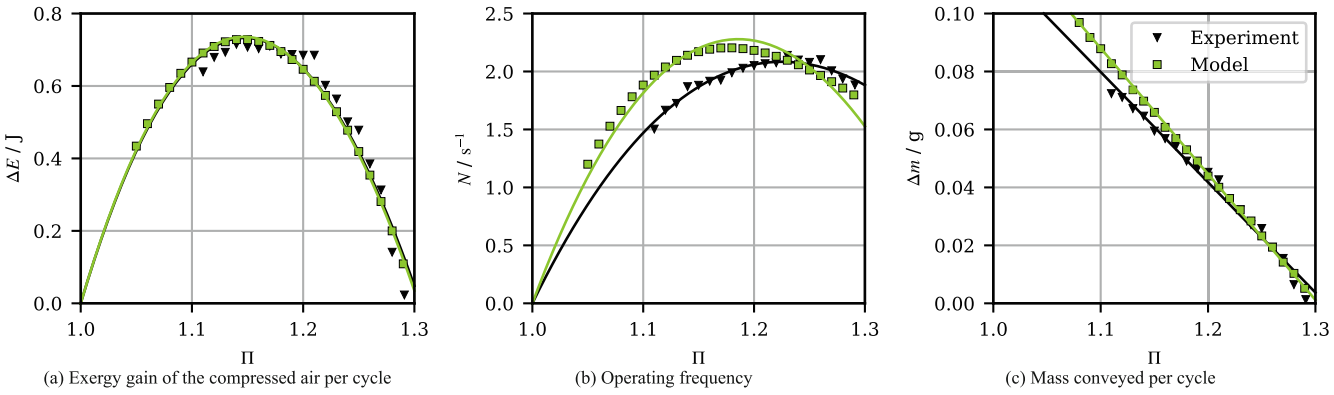

(a) Exergy gain of the compressed air per cycle (b) Operating frequency (c) Mass conveyed per cycle

Fig. 10. Comparison of the experimental operating curve #1 and the calculated operating curve for ambient pressure, $T_h = 295^\circ C$ and $T_c = 8^\circ C$ and fitted functions [38].

operating curve including those obtained at higher inlet pressures can be reproduced by simulations using the same correction factors $f_{leak,1}$ and $f_{leak,2}$. This provides additional support for the principal correctness of the assumed leakage flow model, since it is evidently capable of reproducing the effects of varying operating conditions correctly.

5.1.4. *Influence of the inlet pressure on the performance*

Even though only one stage was built as a prototype, the operating behavior of higher thermocompressor stages within a cascade was to be investigated. Therefore, a variation of the inlet pressure p_k was performed. Of course, this approach excludes pressure variations in the buffers of consecutive stages due to inflow and outflow and thus any kind of mutual interference, but nevertheless, the general influence of the higher inlet pressure on the operating curve can be investigated. The results of an inlet pressure at atmospheric conditions were interpreted as a first stage, which should be operated at its optimum operating point. To visualize the optimum operating point, Fig. 11(a) shows the exergy flow $\dot{E}$ transferred to the compressed air as a function of the pressure ratio. Since $\dot{E}$ equals the product of N and ΔE, the fitted functions displayed as the solid lines represent the product of the corresponding functions as well. The optimum operating point is determined for approximately $\Pi = 1.17$ and is indicated by a vertical dotted line. Assuming steady-state operation of all stages, the inlet pressure of a stage $k+1$ is the outlet pressure of the previous stage k. To represent the second stage $k = 2$, the inlet pressure was therefore set to $p_1 = 1.18$ bar. Because of the constraint of a constant mass flow along the cascade, all subsequent stages must operate at the same mass flow as the first, which is indicated as a horizontal dotted line in Fig. 11(c). Therefore, stage $k = 2$ is assumed to operate at $\Pi_2 = 1.19$. The resulting operating data for the first four stages of a cascade is summarized in Table 3.

Table 3
Operating data for consecutive stages at a mass flow of 0.104 g/s.

Stage k	p_{k-1} / bar	Π_k	N_k / s^{-1}
1	1.01	1.17	1.92
2	1.18	1.19	2.21
3	1.40	1.18	2.37
4	1.66	1.17	2.40

In general, the maximum exergy flow transferred to the compressed air increases as the inlet pressure is increased. However, instead of simply scaling the curves as expected considering Eq. (1), Fig. 11 shows that varying the inlet pressure reduces the maximum pressure ratio because the leakage depends on the absolute pressure difference, which obviously scales with the inlet pressures for a given pressure ratio. Thus, the maximum of the exergy flow transferred to the compressed air is shifted to lower pressure ratios.

Fig. 11(b) and Table 3 indicate that the frequency at the relevant operating points is slightly increasing with increasing inlet pressure, which supports the aforementioned implication of Eq. (11). Because the effectively measured conveyed mass flow is reduced at higher pressure ratios, this effect is expected to be more significant if leakages are reduced. For the same reason, the pressure ratios, at which the same mass flow as in stage 1 is measured, do not increase monotonously with rising inlet pressures.

5.2. *Unsteady operation*

In addition to the steady-state operation, its transient operating capabilities are also of interest. Typically, compressed air systems consist

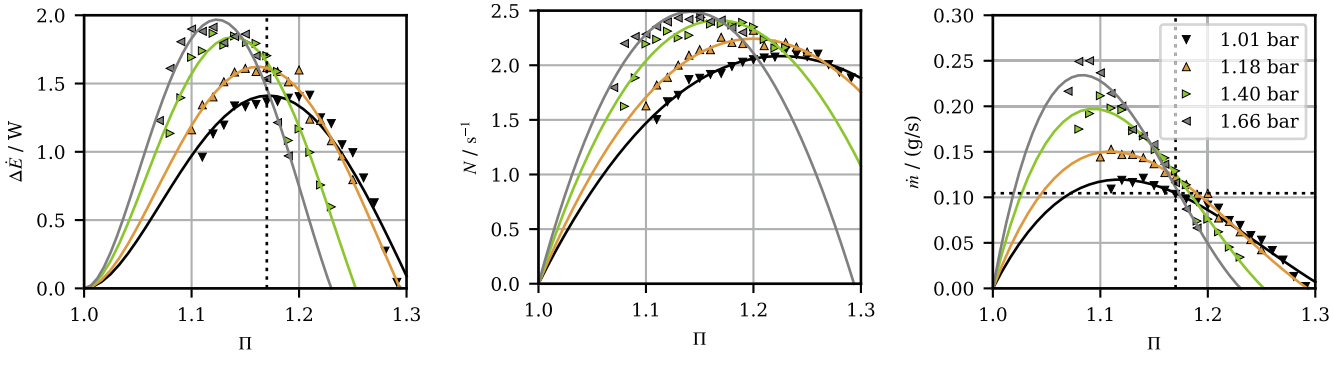

(a) Exergy gain of the compressed air flow (b) Operating frequency (c) Mass flow conveyed

Fig. 11. Measurement results (#1, #4, #8, #10) for various inlet pressures p_k and $T_h = 295^\circ C$ and $T_c = 8^\circ C$ and fitted functions. The dotted lines mark the optimum operating point at $\Pi = 1.17$ of the "first" stage at ambient pressure [38].

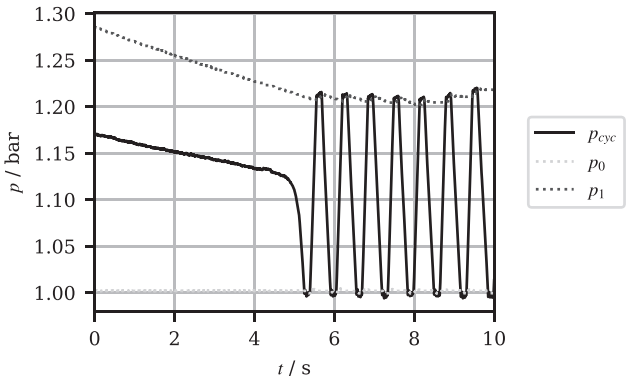

Fig. 12. Pressure course of p_{cyc}, $p_{0,}$ and p_1 for restarting after standstill at T_c = 8 °C and T_h = 295 °C [38].

of a conventional compressor, compressed air treatment equipment, such as filters and dryers, and a storage tank. The latter is filled with air at a certain maximum pressure level. Depending on the type of compressor, the supply may be continuously controlled to match the current demand, or the tank may act as a buffer with fluctuating pressure. Due to the self-control capabilities experimentally demonstrated in the steady-state operation presented in section 5.1, a thermocompressor with an overdriven free displacer could be easily integrated into conventional compressed air systems, since the maximum pressure is thermodynamically limited.

As shown in section 5.1, the machine will continue to operate even when the maximum pressure ratio is reached. Therefore, a thermocompressor cascade of this design will not stop, unless the leakage can be significantly reduced. If this definitely desirable goal should be achieved, it is of interest to know whether a stage can be restarted in the event of a pressure decrease as it may be caused by varying consumption of compressed air. This scenario was realized by filling the outlet buffer via the bypass at standstill of the machine, so that a pressure ratio above Π_{max} is preset. Starting from a pressure of approximately 1.29 bar, p_1 is lowered by opening a valve to the atmosphere. As shown in Fig. 12, the stage starts to operate without any further intervention after undercutting a critical pressure ratio of Π = 1.21. This behavior qualitatively confirms the simulation results presented in [27]. The self-excited restart ability extends the advantageous operation characteristics of such a machine for industrial applications, as no complex external controller is needed for the system, even if a stage stops operating. During the experiments, this feature was intentionally used to start the machine, but it also happened that the machine accidentally restarted due to leakages after a standstill.

6. Conclusion and outlook

Within this contribution, the feasibility of a thermocompressor with an overdriven free-displacer was experimentally proven for the first time. In particular, it was successfully demonstrated that steady-state operation is achieved for a wide range of pressure ratios and inlet pressures. The dependencies of the presented performance characteristics, such as the conveyed mass per cycle and the operating frequency on these agree well with the predictions based on analytical and numerical models. This is also true for the lowest pressure ratio, at which a stable operating point is achieved, which is in good agreement with the lower stability limit predicted by an analytical analysis [27].

The maximum experimentally achievable pressure ratio is significantly reduced due to leakage from the cycle volume and the outlet buffer to the inlet buffer. As a result, the thermocompressor does not stop as originally expected. This finding is advantageous from the practical point of view, since there is no need to restart the cascade in this case. It may be quantitatively reproduced by the presented numerical model, if merely the leakage coefficients are adjusted accordingly.

For higher inlet pressures, the power output in terms of exergy transferred to the compressed air flow is increased as expected. However, the leakage flows are dependent on the absolute pressure differences and thus become even more dominant and further reduce the maximum achievable pressure ratio. Therefore, future developments should focus on a further reduction of the leakage between the displacer rod and the bushings without simultaneously increasing friction.

Furthermore, the design of the guide bushings should also be reconsidered to avoid the water management for lubrication and sealing purposes, particularly since the water flow that can be expected to accumulate by condensation in the higher stages of a cascade would be insufficient anyway. Instead of plastic bushings, dry-running bushings made of bearing bronze may be considered to further reduce the system complexity, thus following the original objective of a simple design targeting a low-cost series production.

With regard to unsteady operation, the demonstration of an automatic restart from an assumed standstill simply by a decreasing outlet pressure is an important finding. In an industrial application, this feature allows an operation without any external control, since such a machine will restart automatically when the pressure in a reservoir drops due to an increased consumption of compressed air. In the future, these investigations should be extended to a cascade of multiple stages to verify that all stages consecutively restart operation, as predicted by numerical simulations [27].

Based on the experience gained in the reported single-stage experiments, a multi-stage cascade should be constructed as a next step to experimentally investigate both its steady-state and unsteady operating characteristics to confirm the predictions by analytical and numerical models, particularly focusing on stability issues, which could not be studied with a single stage. Following the general idea of a cost-efficient machine from the very beginning, the general design, especially the concentric design with an annular gap replacing complex heat exchangers and regenerators, should be pursued and further developed.

Data availability

Datasets related to this article can be found at https://doi.org/10.5281/ZENODO.8289373, an open-source online data repository hosted at ZENODO [38].

CRediT authorship contribution statement

Fabian Fischer: Writing – original draft, Visualization, Validation, Software, Investigation, Data curation. **Hans-Detlev Kühl:** Writing – review & editing, Supervision, Project administration, Funding acquisition, Conceptualization.

Declaration of competing interest

The authors declare that they have no known competing financial interests or personal relationships that could have appeared to influence the work reported in this paper.

Acknowledgments

This research was funded by the German Research Foundation (DFG), grant number KU 755/5-1.

Appendix

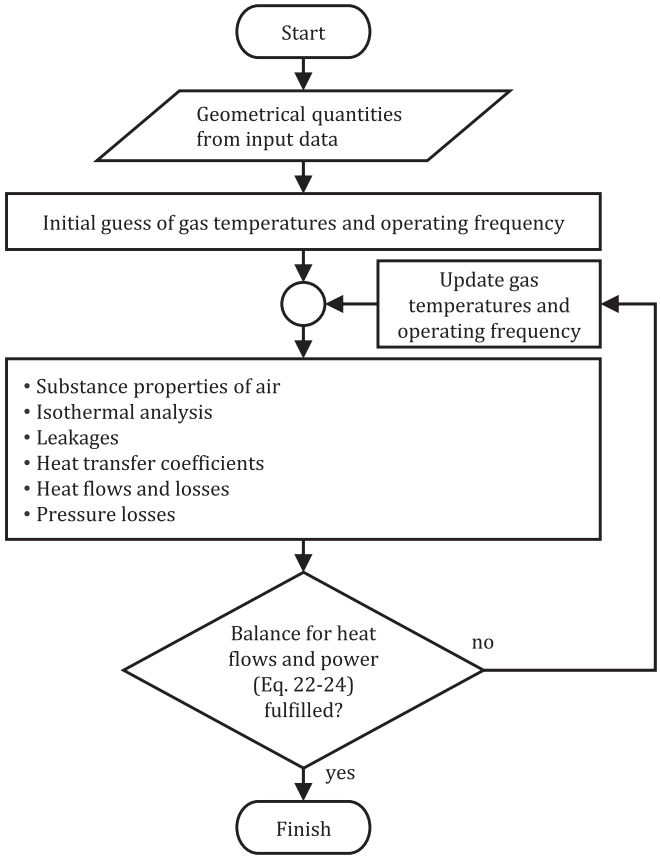

Fig. A1. Flowchart of the calculation model.

Table A1
Instrumentation of the test stand.

Measuring point name	Type of sensor	Model name	Measuring range	Maximum error
FIR-0001	Thermal mass flow meter	Vögtlin GSM-C4TA-BN00	0.2 … 20 ln/min 0.04 … 4 ln/min	±0.3 % of full scale +±0.5 % of reading
GIR-0001	Linear variable differential transformer	AMOS AWM-41-33	0 … 66 mm	0.3 % of full scale
PIR-0011	Pressure transmitter	Kistler 4011A010DSL81-2,0	0 … 10 bar	±0.3 % of full scale
PIR-000X	Pressure transmitter	IFM PT-010-AFG14-A-ZVG/US	0 … 10 bar	±0.5 % of full scale (BFSL)
TIR-0001	Resistance thermometer PT100 Class A	Sontec 800-02 9TT6-045-A-A-4L-S-2,0-ADE	−40 … 180 °C	±0.15 K + 0.2 % of reading
TIR-001X	Thermocouple Type K Class 1	Roessel AL-KB-0,5	0 … 1.100 °C	±1.5 K

Table A2
Data acquisition modules used.

Module name	Description	Measuring points/Outputs
NI cDAQ-9178	8-slot USB Chassis for C Series Modules	NI-9253, NI-9210, NI-9217
NI-9253	50 kS/s/Channel, ±20 mA, 24-Bit, 8-Channel C Series Current Input Module	FIR-0001, GIR-0001, PIR-0011, PIR-0001, PIR-0002
NI-9210	4-Channel, 14 S/s Aggregate, ±80 mV C Series Temperature Input Module for Thermocouples	TIR-0011, TIR-0012, TIR-0013, TIR-0014
NI-9217	4-Channel, 400 S/s Aggregate, 0 Ω to 400 Ω, PT100 RTD C Series Temperature Input Module	TIR-0001
NI USB-6211	16 Analog Input (16-Bit, 250 kS/s), 2 Analog Output (250 kS/s), 4 Digital Input, 4 Digital Output USB Multifunction Input/Output Device	Heater control, Control valve

Table A3
Input data for simulation model.

value	unit	variable name	description
48.6	mm	s	stroke
82.5	mm	d_D	diameter displacer
1.25	mm	s_D	Wall thickness displacer
256.	mm	l_D	Length of displacer
1.2	mm	s_{gap}	Gap width
1.15	mm	s_C	Wall thickness cylinder
88.	mm	l_c	Length cooler
1.	–	f_c	Area factor for displacer base
85.	mm	l_h	Length heater
1.25	–	f_h	Area factor for displacer dome
0.058769	–	ρ	Displacer rod ratio
10.96	cm3	$V_{d,c,add}$	Additional dead volume cold cylinder volume
10.96	cm3	$V_{d,h,add}$	Additional dead volume hot cylinder volume
8.5	mm	$d_{v,in}$	Inlet valve hole diameter
5.5	mm	$d_{v,out}$	Outlet valve hole diameter bore
4	–	n_{in}	Number of inlet valves
4	–	n_{out}	Number of outlet valves
1.0	mm	h_{in}	Opening of inlet valves
1.3	mm	h_{out}	Opening of outlet valves
35.	mm	l_{b1}	Length of bushing 1 (between cycle volume and inlet buffer)
25.	mm	l_{b2}	Length of bushing 2 (between outlet buffer and inlet buffer)
0.028	mm	$s_{b,gap1}$	Gap between bushing 1 and displacer rod
0.014	mm	$s_{b,gap2}$	Gap between bushing 2 and displacer rod
2.1	kg	m_D	Displacer mass

Table A4
Overview of measured operating curves [38].

		Set point				
#	Source Name	p_0/bar	T_h/°C	T_c/°C	LVDT installed?	In Figures
1	VVM_exp_100_295_08_stat_BK_008	1.00	295	8	No	Fig. 9, Fig. 10, Fig. 11
2	VVM_exp_100_295_08_stat_BK_020	1.00	295	8	No	Fig. 9
3	VVM_exp_100_295_08_stat_BK_022	1.00	295	8	Yes	Fig. 9
4	VVM_exp_118_295_08_stat_BK_001	1.18	295	8	No	Fig. 11
5	VVM_exp_118_295_08_stat_BK_021	1.18	295	8	Yes	
6	VVM_exp_118_295_08_stat_BK_023	1.18	295	8	Yes	
7	VVM_exp_118_295_08_stat_BK_024	1.18	295	8	Yes	
8	VVM_exp_140_295_08_stat_BK_001	1.40	295	8	No	Fig. 11
9	VVM_exp_140_295_08_stat_BK_025	1.40	295	8	Yes	
10	VVM_exp_166_295_08_stat_BK_001	1.66	295	8	No	Fig. 11
11	VVM_exp_166_295_08_stat_BK_026	1.66	295	8	Yes	

References

[1] M. Unger, P. Radgen, Energy Efficiency in Compressed Air Systems: A review of energy efficiency potentials, technological development, energy policy actions and future importance, in *Proceedings of the 10th International Conference on Energy Efficiency in Motor Driven Systems (EEMODS' 2017)* (ed P. Bertoldi), 6.-8.09.2017, Rome, Italy. Publications Office of the European Union, Luxembourg (2018), pp. 207–233.

[2] S. Brückner, L. Miró, L.F. Cabeza, M. Pehnt, E. Laevemann, Methods to estimate the industrial waste heat potential of regions – A categorization and literature review, Renew. Sustain. Energy Rev. 38 (2014) 164–171, https://doi.org/10.1016/j.rser.2014.04.078.

[3] L. Miró, S. Brückner, L.F. Cabeza, Mapping and discussing Industrial Waste Heat (IWH) potentials for different countries, Renew. Sustain. Energy Rev. 51 (2015) 847–855, https://doi.org/10.1016/j.rser.2015.06.035.

[4] M. Papapetrou, G. Kosmadakis, A. Cipollina, U. La Commare, G. Micale, Industrial waste heat: Estimation of the technically available resource in the EU per industrial sector, temperature level and country, Appl. Therm. Eng 138 (2018) 207–216, https://doi.org/10.1016/j.applthermaleng.2018.04.043.

[5] C. Forman, I.K. Muritala, R. Pardemann, B. Meyer, Estimating the global waste heat potential, Renew. Sustain. Energy Rev. 57 (2016) 1568–1579, https://doi.org/10.1016/j.rser.2015.12.192.

[6] F. Fischer, H.-D. Kühl, Analytical model for an overdriven free-displacer thermocompressor, Appl. Therm. Eng 185 (2021) 116251, https://doi.org/10.1016/j.applthermaleng.2020.116251.

[7] V. Bush, Apparatus for Compressing Gases. US Patent 2,157,229, filed Jul. 17, 1935 and issued May. 9 (1935), 1939.

[8] E. Blagin, I. Uskov, E. Kuznetsova, A. Dovgyallo, Development of thermocompressor mathematical model considering hydraulic losses in regenerator, in: *2020 International Multi-Conference on Industrial Engineering and Modern Technologies (FarEastCon)* (ed Institute of Electrical and Electronics Engineers), 06.-09.10.2020, Vladivostok, Russia. IEEE (2020), pp. 1–7. 10.1109/FarEastCon50210.2020.9271643.

[9] S. Thomas, E.J. Barth, Active Stirling Thermocompressor: Modelling and effects of controlled displacer motion profile on work output, Appl. Energy 327 (2022) 120084, https://doi.org/10.1016/j.apenergy.2022.120084.

[10] W. Ji, X. Xue, J. Wang, Y. Zhou, L. Chen, W. Zhu, Coupling study of a novel thermocompressor driven pulse tube refrigerator, Appl. Therm. Eng 51 (1–2) (2013) 630–634, https://doi.org/10.1016/j.applthermaleng.2012.10.034.

[11] R. Ibsaine, J.-M. Joffroy, P. Stouffs, Modelling of a new thermal compressor for supercritical CO_2 heat pump, Energy 117 (2016) 530–539, https://doi.org/10.1016/j.energy.2016.07.017.

[12] J. Wang, C. Pan, K. Luo, L. Chen, J. Wang, Y. Zhou, Thermal analysis of Stirling thermocompressor and its prospect to drive refrigerator by using natural working fluid, Energy Convers. Manag. 177 (2018) 280–291, https://doi.org/10.1016/j.enconman.2018.09.068.

[13] F.X. Eder, Concept, theory and performance of a thermo-hydraulic engine, in: Proceedings 6th ISEC, Eindhoven, NL, 1993, pp. 143–148.

[14] J.A. Riofrio, Design and Implementation of a Free Piston Compressor. Vanderbilt University Master Thesis(2005) .

[15] J.A. Riofrio, Design, Modeling and Experimental Characterization of a Free Liquid-Piston Engine Compressor with Seperated Combustion Chamber. Vanderbilt University PhD Thesis (2008).

[16] J.C. Moise, M.I. Rudnicki, R.J. Faeser, Development of a thermocompressor power system for implantable artificial heart application, in: Proc. 8th IECEC (ed American Society of Mechanical Engineers), 1973, pp. 511–535.

[17] W.R. Martini, The Thermocompressor and its application to artificial heart power, in: Proc. 4th IECEC, American Chemical Society, Washington, D.C., USA, 1969, pp. 107–114.

[18] M.J. Edwards, Design, Modeling, and Performance of Miniature Reciprocating Thermocompressor. Oregon State University Master Thesis (2005).

[19] W.-Y. Lin, X.-H. Wu, J.-L. Yang, L.-W. Yang, Experimental study and numerical analysis of thermocompressors with annular regenerators, Int. J. Refrig. 36 (4) (2013) 1376–1387, https://doi.org/10.1016/j.ijrefrig.2013.02.006.
[20] X.H. Wu, L.W. Yang, J.L. Yang, W.Y. Lin, Experimental study of linear motor direct-driven thermocompressor, AMR 732–733 (2013) 1147–1152, https://doi.org/10.4028/www.scientific.net/AMR.732-733.1147.
[21] M.E. Hofacker, N.S. Kumar, E.J. Barth, Dynamic simulation and experimental validation of a single stage thermocompressor for a pneumatic ankle-foot orthosis, in: *Proceedings of the ASME/BATH Symposium on Fluid Power and Motion Control 2013 (FPMC2013): Presented at ASME/BATH 2013 Symposium on Fluid Power and Motion Control, October 6-9, 2013, Sarasota, Florida, USA*, 6.10.2013-9.10.2013 (2014), Sarasota, FL, USA. ASME, New York. 10.1115/FPMC2013-4483.
[22] A. Winkelmann, E.J. Barth, Design, modeling, and experimental validation of a stirling pressurizer with a controlled displacer piston, IEEE/ASME Trans. Mechatron. 21 (3) (2016) 1754–1764, https://doi.org/10.1109/TMECH.2015.2499706.
[23] E. Blagin, S. Korneev, A. Lopatin, D. Sarmin, Experimental Investigation of Thermocompressor, in *2021 International Scientific and Technical Engine Conference (EC)* (ed Institute of Electrical and Electronics Engineers), 23.-25.06.2021, Samara, Russian Federation. IEEE (2021), pp. 1–5. 10.1109/EC52789.2021.10016836.
[24] A.P.M. Glassford, An Oil free Air Compressor based on the Stirling Cycle, Massachusetts Institute of Technology Master Thesis, 1962.
[25] S. Thomas, E.J. Barth, Stirling thermocompressor: lumped parameter modeling and experimental impact of displacer motion profile on work output, in: *ASME/BATH 2019 Symposium on Fluid Power and Motion Control*, 07.10.2019 - 09.10.2019, Longboat Key, Florida, USA. American Society of Mechanical Engineers. (2019) 10.1115/FPMC2019-1683.
[26] S. Thomas, E.J. Barth, Multi-stage modeling of a stirling thermocompressor, in: Proceedings of the ASME/BATH 2017 Symposium on Fluid Power and Motion Control (FPMC2017), 16.10.2017, Sarasota, FL, USA, 2017, https://doi.org/10.1115/FPMC2017-4320.
[27] F. Fischer, S. Peveling, H.-D. Kühl, Simulation and stability analysis of a thermocompressor cascade with overdriven free displacers, Therm. Sci. Eng. Prog. 44 (2023) 102037, https://doi.org/10.1016/j.tsep.2023.102037.
[28] F. Fischer, H.-D. Kühl, Generation of compressed air by cascaded thermocompressors – project status, E3S Web Conf. 313 (2021) 4003, https://doi.org/10.1051/e3sconf/202131304003.
[29] A.P.M. Glassford, Adiabatic cycle analysis for the valved thermal compressor, J. Energy 3 (5) (1979) 306–314, https://doi.org/10.2514/3.48007.
[30] H. Karabulut, Thermodynamic Analysis Of Bush Engine, Gazi Univ. J. Sci. 16 (1) (2003) 135–144.
[31] G. Walker, Stirling-cycle Machines, Clarendon Press, Oxford, 1973, 0198561121.
[32] W. Eifler, E. Schlücker, U. Spicher, G. Will, *Küttner Kolbenmaschinen: Kolbenpumpen, Kolbenverdichter, Brennkraftmaschinen*, mit 40 Tabellen sowie zahlreichen Übungen und Beispielen mit Lösungen, 7th edn, Vieweg + Teubner, Wiesbaden, 2009, 978-3-8351-0062-6.
[33] G. Samland, Kolbenkompressorventile aus der Sicht eines Kompressor- und Ventilherstellers, Industriepumpen + Kompressoren 8 (1) (2002) 19–23.
[34] M. Beyer, Do you know the accuracy of your pressure sensor?: Find your way out of the waze of accuracy data? Sensor Magazin. (2008).
[35] Verein Deutscher Ingenieure, VDI-Wärmeatlas, 11th ed., Springer Vieweg, Berlin, Heidelberg, 2013, 9783642199813.
[36] G. Woschni, Beitrag zum Problem des Wärmeüberganges im Verbrennungsmotor, MTZ Motortechnische Zeitschrift 26 (1965) 128–133.
[37] I. Urieli, D.M. Berchowitz, *Stirling Cycle Engine Analysis*, Adam Hilger Ltd, Bristol, 1984, 0-085274-435-2.
[38] F. Fischer, H.-D. Kühl, Experimental data for a single-stage overdriven free-displacer thermocompressor (1.0) [Data Set]. Zenodo (2023). 10.5281/ZENODO.8289373.
[39] Becker International Data Sheet DT 4.2 Rotary Vane Compressors. https://main.becker-international.com/zfiles/allgemein/1639674320_ds_Becker_DT_4.2_Compressors_en.pdf (15 January 2024).